Materials Science & Engineering A 833 (2022) 142362

Contents lists available at ScienceDirect

Materials Science & Engineering A

journal homepage: www.elsevier.com/locate/msea

Superelastic behavior and elastocaloric effect in a $Ni_{51.5}Fe_{21.5}Ga_{27.0}$ ferromagnetic shape memory single crystal under compression

F. Masdeu [a], J. Pons [b], J. Torrens-Serra [b,*], Y. Chumlyakov [c], E. Cesari [b]

[a] Departament d'Enginyeria Industrial i Construcció, Universitat de les Illes Balears, Ctra. de Valldemossa, Km 7.5, E07122, Palma de Mallorca, Spain
[b] Departament de Física, Universitat de les Illes Balears, Ctra. de Valldemossa, Km 7.5, E07122, Palma de Mallorca, Spain
[c] Tomsk State University, Lenina Street, 634050, Tomsk, Russia

ARTICLE INFO

Keywords:
Martensitic transformation
Ni–Fe-Ga
Superelasticity
Elastocaloric effect

ABSTRACT

$Ni_{51.5}Fe_{21.5}Ga_{27.0}$ single crystals have been subjected to different heat treatments resulting in a different degree of $L2_1$ ordering. Superelastic response has been measured at different temperatures in compression mode. The mechanical behavior strongly depends on axis orientation. In the [001] direction, perfect superelasticity over a wide range of temperatures is found. For the [110] orientation, the material fails by brittle fracture short above austenite transformation finish temperature, A_f. A linear dependence of the critical stress with temperature has been found in agreement with Clausius-Clapeyron equation. The slope does not significantly change with the degree of order, but it is notably affected by the crystal orientation. The microstructure of the samples after mechanical tests has been studied by transmission electron microscopy. The superelastic cycling produces dislocations with a Burgers vector that suggests local microplastic deformation of the martensitic phase. Finally, the adiabatic temperature change has been used to chacterize the elastocaloric effect in this alloy. The adiabatic cooling is found to be larger in the [110] than in the [001] orientation at 240 K. However, the brittleness of [110] samples avoid testing the adiabatic temperature change at room temperature. The adiabatic cooling in [001] orientation decreases systematically with temperature, which is related to decrease of the strain and entropy change of transformation.

1. Introduction

Shape memory alloys (SMA) have attracted an enormous interest due to their excellent functional properties that find general applications as sensors [1] or actuators [2,3], particular applications in fields like construction [4], aerospace and medicine [5] and more recently, as caloric materials for solid-state refrigeration [6–11]. These materials present a reversible martensitic transformation from a high symmetry parent phase to a low symmetry martensitic phase either by cooling below a certain temperature or by the application of load. The stress-induced phase transformation is accompanied by the generation of macroscopic strain, which can be fully recovered upon unloading (pseudo- or superelasticity effect). The most commercially used of this class of materials are the Ni–Ti alloys. In 1996 Ullakko and co-workers [12] reported the discovery of the so-called Ferromagnetic Shape Memory Effect (FSME) in an off-stoichiometric Heusler-type Ni_2MnGa alloy. Large values of strain (up to 12% [13]) can be induced by the application of magnetic field around 1 T. The strain is not produced by a field-induced martensitic transformation but by reorientation from single-variant or self-accomodated multivariant martensite to another single-variant orientation when the field is applied. In this case, no recovery is obtained by the sole removal of the field, being necessary a bias stress to achieve reversible strain. However, the brittle behavior of Ni–Mn-Ga alloys motivated researchers to uncover other magnetic alloys such as Ni-Mn-Al [14], Co-Ni-Ga [15], Co-Ni-Al [16] and Ni–Fe-Ga [17], with enhanced mechanical properties in comparison to Ni–Mn-Ga alloys, especially ductility, due to the formation of small amounts of a ductile second phase (γ phase) [18]. The FSME in Ni–Fe-Ga alloys was firstly reported by Oikawa et al. [17]. Since then, a large number of papers have appeared dealing with the influence of composition, ageing and atomic order in the martensitic transformation and mechanical properties in both single crystals [19–24] and polycrystalline alloys [25–29]. Despite the promising mechanical properties, the variant reorientation mechanism is hindered in this alloy system, compared to Ni–Mn-Ga, as it takes place under too high stress levels, above the magnetostress, which makes not feasible their applications based on the

* Corresponding author.
E-mail address: j.torrens@uib.es (J. Torrens-Serra).

https://doi.org/10.1016/j.msea.2021.142362
Received 27 September 2021; Received in revised form 16 November 2021; Accepted 17 November 2021
Available online 20 November 2021

FSME [30]. Small additions of Co increase the magnetostress, allowing magnetic field–induced strain up to 0.7% [31,32]. However, the performance is still well below Ni–Mn-Ga alloys [13]. On the other hand, Ni–Fe-Ga presents excellent conventional shape memory effect and superelasticity. In Ni–Fe-Ga single crystals, the mechanical properties depend on the crystal orientation [19,33,34], testing mode [22], temperature [20,35] and amount of γ phase present in the alloy [36,37]. Sutou and co-workers [20] reported the achievement of 12% reversible stress-induced strain, comparable to Ni–Ti alloys, in single crystals oriented in the [001] direction during tensile experiments. The stress-induced transformation proceeds in different steps related to different martensitic phases induced, depending on temperature and load, which are generally different from the thermally-induced martensite. The relationship between the macroscopic stress-strain curve and the local strains and different martensitic phases formed was deeply studied in Ref. [38]. Finally, another interesting functionalty of Ni-(Co)–Fe-Ga alloys has been recently introduced, based on the possibility to reach the critical point in this material. In the postcritical regime, the discontinuous (first order) martensitic transformation is replaced by a continuous process where the material experiences large recoverable strains completely anhysteretic [39,40].

In the recent years, the search for caloric materials for solid-state refrigeration by either magnetocaloric (MCE) or elastocaloric (eCE) effects drives a new interest for Shape Memory Alloys [10,41]. The large entropy change associated to the martensitic transformation makes them suitable candidates to replace conventional magnetic materials, often containing rare-earth elements. Although Ni–Fe-Ga exhibits low magnetic entropy change and does not seem to be a good candidate for MCE [42], the large entropy change of the martensitic transformation and good ductility allow this alloy to be applied in eCE technology [8,43–46]. Therefore, the study of the stress-induced martensitic transformation under compression has become a matter of high interest [47–50]. In particular, there is a lack of detailed microstructural studies of the defects generated by the mechanical cycling, which is an important topic to understand the fatigue behavior under prolongued cycling.

In this paper we perform mechanical tests in a $Ni_{51.5}Fe_{21.5}Ga_{27.0}$ single crystal with different atomic order degrees in a broad temperature range and in two different orientations. The alloy composition has been chosen to undergo the martensitic transformation below room temperature, to facilitate the detailed microstructural study by TEM with the material in austenite state at room temperature. Crystallographic, microstructural and functional aspects will be discussed.

2. Materials and methods

A single crystalline ingot of composition $Ni_{51.5}Fe_{21.5}Ga_{27.0}$ (at%) was grown by Bridgman's method. Two sets of prismatic samples with dimensions $9 \times 4 \times 4$ mm^3 were spark cut from the ingot with the long axis oriented along the [001] and along the [110] directions of the austenitic phase, respectively. The as-cast material after the single crystal growth exhibits the martensitic transformation. However, as this state is difficult to reproduce, some samples for each direction of the loading axis were encapsulated in quartz ampoules under low pressure argon atmosphere and solution heat treated (SHT) at 1420 K for 1 h followed by water quenching. In order to study the effect of atomic ordering on the mechanical response of the alloy and considering the results of ref. [27], as cast and SHT samples were subsequently heat treated at 970 K for 20 min followed by water quench, to retain a low degree of $L2_1$ atomic order. Another sample was treated at 1070 K for 20 min followed by a slow air cooling in a porcelain crucible, which results in a high $L2_1$ atomic order degree of the austenitic phase [27]. Table 1 summarizes the heat treatments and crystalline orientation of the studied samples. Characteristic temperatures and transformation enthalpy changes were obtained from differential scanning calorimetry (DSC, TA Instruments DSC2920 model) using small samples with tens of mg of mass at 10 K/min. Structural and microstructural characterization was performed

Table 1
Thermal treatments and crystallographic orientation for mechanical testing of the studied samples.

Sample	Initial treatment	Ordering treatment	Orientation
A	'as cast'	970 K 20min + water quench	[001]
B	'as cast'	1070 K 20min + slow cooling	[001]
C	1420 K 1h + water quench	970 K 20min + water quench	[001]
D	'as cast'	970 K 20min + water quench	[110]
E	1420 K 1h + water quench	970 K 20min + water quench	[110]

by Optical microscopy (OM) and Transmission Electron Microscopy (Hitachi H600 at 200 kV). The TEM discs were double jet electropolished using a mixture of 20% perchloric acid in ethanol under 10 V at room temperature. The density (ρ) of the alloy was determined from the mass and dimensions of a prismatic sample.

Mechanical tests in compression along the long axis of different samples with [001] or [110] orientations were carried out using a Zwick Z100 testing machine. The stress-induced transformation and superelasticity effect was studied with crosshead speed of 0.3 mm/min, resulting in a strain rate of $6{\cdot}10^{-4}$ s^{-1}. Each sample was cycled at different temperatures, starting from 240 K and increasing the temperature by steps of 10 K (performing two loading/unloading cycles at each temperature), until the sample collapsed by plastic deformation or fracture (except for sample A, which was preserved from collapsing). The elastocaloric effect was characterized from the temperature change measured during loading and quasi-adiabatic unloading using a K-type thermocouple attached to the sample surface. The sample was set at the measuring temperature and loaded at a strain rate of $6{\cdot}10^{-3}$ s^{-1} until the complete transformation, then hold for 120 s at constant load and finally unloaded to zero stress at a strain rate of $6{\cdot}10^{-2}$ s^{-1}, i.e 100 times faster than standard conditions applied in superelasticity studies, to achieve a quasi-adiabatic process.

3. Results and discussion

3.1. Initial microstructure and thermal response of heat-treated samples

DSC thermograms during cooling and heating of all the samples are presented in Fig. 1. All of them show single peaks for the direct and reverse martensitic transformation from the $L2_1$ parent phase to the thermally induced martensite. The latter was identified by means of electron diffraction as a 5-layered (10M) martensite, as shown in Fig. 2 (a), in agreement with previous reports in similar alloys for both

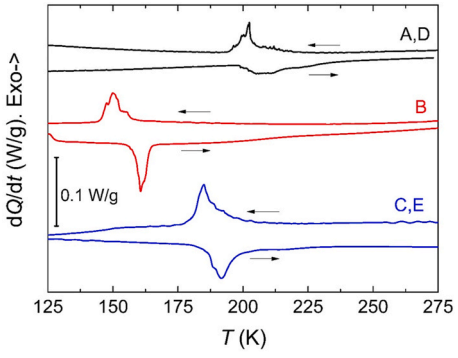

Fig. 1. DSC thermograms of different $Ni_{51.5}Fe_{21.5}Ga_{27.0}$ samples: samples A and D, black line; sample B, red line; sample C and E, blue line. (For interpretation of the references to color in this figure legend, the reader is referred to the Web version of this article.)

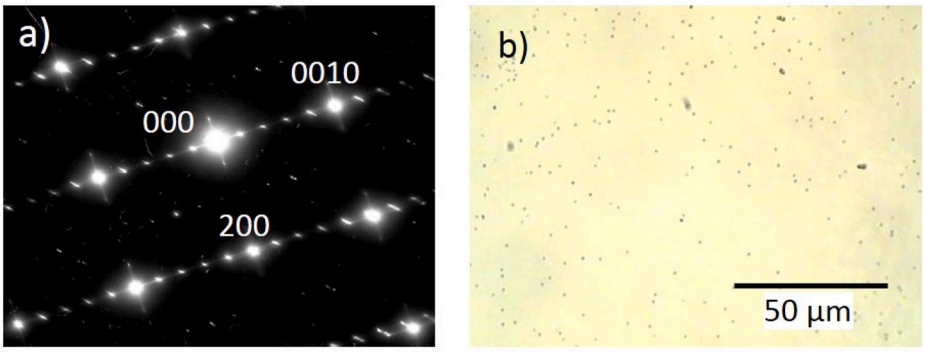

Fig. 2. (a) Elecron diffraction pattern of the as-cast sample obtained at 120 K showing the 10M structure of martensite. (b) Optical microscopy image of the as-cast sample containing small oxide inclusions.

polycrystalline [17] and single crystal [20] forms. Fig. 2(b) shows the microstructure of the as-cast alloy at room temperature, which is composed of the $L2_1$ parent phase with a homogeneous distribution of submicrometric (100–200 nm) inclusions of oxide particles formed during alloy casting. Samples solution heat treated at 1420 K present a similar microstructure. These inclusions are considered to play an irrelevant role in this study.

The characteristic martensitic transformation temperatures (MTTs) and transformation enthalpy change for both direct and reverse transitions obtained from DSC are listed in Table 2. Different conclusions can be drawn from the obtained results. Firstly, the MTTs of sample B, submitted to slow air cooling from 1070 K, are decreased by ~ 50 K in relation to samples water quenched from 970 K (samples A, D), in agreement with ref. [27]. In that work, this effect was related to the increase of the $L2_1$ atomic order degree after slow air cooling. In the same way, water quenching generates some heterogeneity in the atomic order throughout the sample volume, resulting in larger transformation temperature ranges (calculated as $\Delta M = M_s - M_f$ and $\Delta A = A_f - A_s$) compared to air cooling, as shown in Table 2. Finally, there is a detectable effect of the initial solution heat treatment at 1470 K (samples C, E), compared to the as-cast state and identical subsequent ordering treatment (samples A, D). As seen in Table 2 and Fig. 1, the initial SHT shifts the martensitic transformation to lower temperatures (M_s decreases by 11 K, whereas the shift in A_s is as large as 18 K); expands the transformation ranges ΔM and ΔA by 6 and 8 K, respectively, and decreases the transformation hysteresis (measured as the difference between direct and reverse transformation peak temperatures, $\Delta T = T_M - T_A$) from 11 to 7 K. These results indicate that the excess of quenched-in vacancies after SHT slightly enhances the degree of atomic order achieved after the subsequent ordering treatment and its heterogeneity within the material.

3.2. Superelastic response

Fig. 3 shows the stress-strain curves in compression along the [001] direction for samples A, B, C, tested in a broad temperature range. Full recovery of the strain upon unloading, *i.e.* perfect superelastic effect, is observed in all cases, except for the tests done at 326 K in sample B and 376 K in sample C (up to stress levels around 700 MPa), where small irrecoverable strains start to appear after unloading. The "plateau" corresponding to the martensitic transformation exhibits some stress undulations that could be indicative of intermartensitic transformations. In fact, the A↔10M↔14M or A↔14M↔2M transformation paths were suggested in Ref. [23] for $Ni_{54}Fe_{19}Ga_{27}$ single crystals in compression along the [001] orientation, the former path being only for low temperature and stress levels. However, other works for Ni–Fe-Ga alloys in this testing mode and orientation do not report intermartensitic transitions [51,52]. Another origin of the stress undulations could be related to friction with the compression plates. The sample starts to transform to a single martensite variant, which causes a macroscopic shear and a lateral shift against the compression plates. When a certain degree of strain and macroscopic shear is reached, the accumulated friction would stop the growth of the compression variant and other variants would start to form to reduce the macroscopic shear, which causes the stress fluctuations. The validity of these possibilities should be confirmed by in-situ structural observations under stress.

The transformation strain (quantified as the width of the transformation 'plateau') decreases with temperature for the three samples, whereas the slope of the 'plateau' increases with temperature, suggesting a hardening effect of the transformation. However, careful inspection of the curves shows that the stress range in which the stress-induced martensitic transformation takes place turns out to be approximately the same for most of temperatures in each sample. Therefore, the apparent increase of the 'plateau' slope is mostly due to the decrease of the transformation strain with temperature, instead of a real hardening effect of the transition when temperature increases.

Fig. 3 (d) compares the detailed mechanical behavior of the three samples with different atomic order degree. To allow for a proper comparison, the curves corresponding to an approximately equal distance from each M_s temperature (~100 K above M_s) are shown. The most remarkable difference is the larger stress range of transformation (slope of the 'plateau') for the quenched samples A and C, compared to the slowly cooled sample B. This is in agreement with the thermal transformation data (Fig. 1, Table 2) and is attributed to the larger inhomogeneity of the atomic order degree throughout the sample volume retained after water quenching in samples A and C. In addition, sample B exhibits a stress hysteresis between direct and reverse transitions of about 30 MPa, while this is around 20 and 15 MPa for samples A and C, respectively.

Fig. 4 presents the stress-strain curves in compression along the

Table 2
Values of the martensitic transformation temperatures (M_s, M_f, A_s and A_f), transformation ranges ($\Delta M = M_s - M_f$, $\Delta A = A_f - A_s$), peak temperatures of the direct and reverse martensitic transformation (T_M and T_A), transformation hysteresis ($\Delta T = T_M - T_A$) and transformation enthalpy change (ΔH) for the studied samples.

Sample	M_s (K)	M_f (K)	ΔM (K)	A_s (K)	A_f (K)	ΔA (K)	T_M (K)	T_A (K)	ΔT(K)	ΔH (J·g^{-1})
A, D	215	192	23	199	235	36	203	214	11	3.5
B	160	143	17	154	169	15	150	161	11	2.8
C, E	204	175	29	181	225	44	185	192	7	3.6

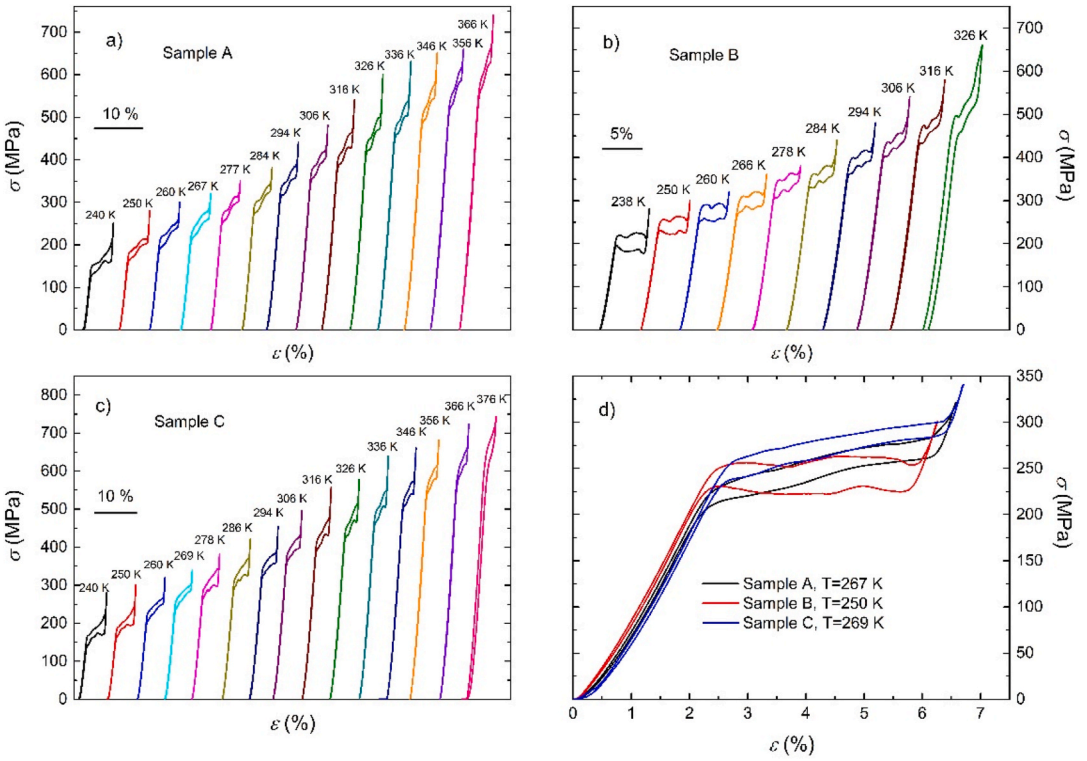

Fig. 3. Stress-strain curves registered at different temperature for samples tested along [001] direction: (a) sample A, (b) sample B and (c) sample C. (d) Comparison of the stress-strain superelastic cicles, performed at the same distance in temperature above M_s.

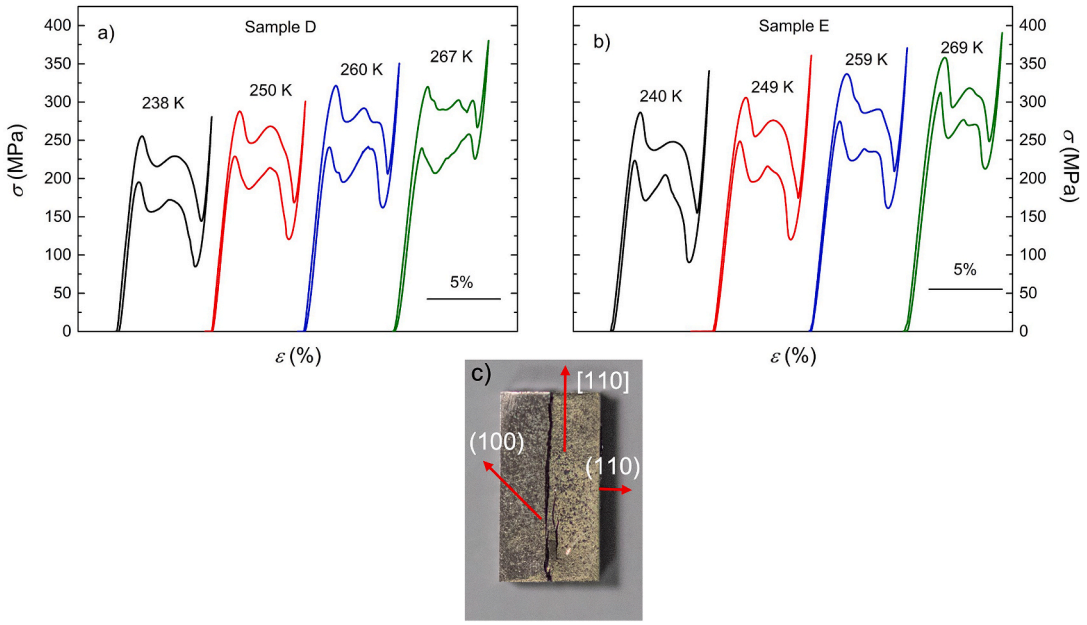

Fig. 4. Stress-strain curves registered at different temperatures for samples tested along [110] direction: (a) Sample D and (b) sample E. (c) Picture of the fracture occurred in the sample during loading along the [110] direction. Perpendicular planes are also indexed.

[110] direction for samples D and E. Both samples present very similar mechanical behavior, showing again perfect superelasticity with recoverable strains of ~ 5%. The initial solution heat treatment at 1470 K does not modify the form of the mechanical curves but causes a shift of the critical stress for transformation that will be discussed later. In both cases, the curves show a very irregular 'plateau' with a large drop and fluctuation of the stress as the strain progresses during loading. Likewise, the retransformation from martensite to austenite during unloading follows a path rather parallel to that of loading. Moreover, only four temperatures could be tested, as both samples collapsed after few cycles (between 8 and 10) by brittle fracture propagated along the compression direction (Fig. 4(c)). This behavior is considerably different from that observed in [001] samples (Fig. 3), but it goes in the same line as previous work reported in literature. A clear two-step transition A↔10M/14M↔2M with no stress drop was reported for the transformation induced in the [110] orientation at stress levels below 100

MPa, *i.e.* close to the M_s temperature [51,53]. However, the reported stress-strain curves at higher stress levels are very similar to those of Fig. 4 [54–56]. The large drop of the stress after the beginning of the transformation has been attributed to the burst-like character of the transformation and to interphase stresses between 14M and 2M [54–56].

The temperature dependences of the critical stress to start the transformation, σ_c, and transformation strain, ε, deduced from the stress-strain curves are plotted in Fig. 5 for all samples. A good linearity is found for both parameters in the studied orientations. The temperature dependence of the critical stress follows the well-known Clausius-Clapeyron equation [57]:

$$\frac{d\sigma_c}{dT} = -\frac{\rho \cdot \Delta S}{\varepsilon}$$

where ρ is the mass density and ΔS is the transformation entropy change. The density of the alloy (in austenite state) has been estimated as 8380 kg m^{-3}, whereas the transformation entropy change can be estimated from calorimetry data as $\Delta S = \Delta H/T_M$, where ΔH is the transformation enthalpy change and T_M is the DSC peak temperature, both for the direct transformation. The value of strain, ε, in the Clausius-Clapeyron equation has been taken from extrapolation of the data in Fig. 5 (b),(d) to the M_s value of each sample. The results obtained are shown in Table 3, where a good agreement between theoretical and experimental values of the slope $d\sigma_c/dT$ can be observed.

Although the critical stress values follow different lines for samples with different ordering degree, similar slopes are found in all samples with an equal crystallographic compresson axis. However, the orientation has a significant effect on the slope $d\sigma_c/dT$, which decreases from 3.2 to 3.5 MPa K^{-1} for the [001] direction to 2.6–3.0 MPa K^{-1} for the [110] (note that only 3 points were used in the fitting of sample D, which increases the uncertainity on the value of the slope). This is in good agreement with literature, where values of 3.3 MPa K^{-1} [19] or 2.9 MPa K^{-1} [34] are reported for [001] and 2.2 MPa K^{-1} [19] for [110] orientation in $Ni_{54}Fe_{19}Ga_{27}$ alloys under compressive stress. Moreover, as shown in Fig. 5(a), there is a systematic shift of the critical stress lines for samples B and C compared to sample A, by ~ 80 MPa and ~ 25 MPa, respectively. Considering the average Clausius-Clapeyron slope for [001] direction, such shifts in σ_c correspond to a decrease of M_s values by ~ 25 K and ~ 8 K, respectively. Similarly, for the [110] orientation, the line for sample E is shifted above that of sample D by ~ 25 MPa (Fig. 5(c)), corresponding again to a decrease of M_s by ~ 8 K. As discussed in the previous section, these changes in transformation stress and temperatures can be attributed to the different $L2_1$ order degree of the samples.

Table 3
Values of transformation entropy change calculated as $\Delta S = \Delta H/T_M$, experimental values of the transformation strain, ε, extrapolated to the M_s temperature, together with the theoretical and experimental values of $d\sigma_c/dT$ obtained from the Clausius-Clapeyron equation and from the slopes of Fig. 5(a) and (c), respectively.

Sample	Orientation	ΔS (J·kg^{-1}·K^{-1})	ε	$(d\sigma_c/dT)_{CC}$ (MPa·K^{-1})	$(d\sigma_c/dT)_{exp}$ (MPa·K^{-1})
A	[001]	17.2	0.046	3.1	3.4
B	[001]	18.7	0.051	3.1	3.2
C	[001]	19.4	0.048	3.4	3.5
D	[110]	17.2	0.055	2.6	3.0
E	[110]	19.4	0.058	2.8	2.6

As shown in Fig. 5(b) and (d), the transformation strain decreases with temperature for all samples tested, as also observed in Ref. [19]. This effect could be due to the change of the martensite lattice parameters with temperature. In fact, Glavatska et al. [58,59] reported a notable temperature evolution of the lattice parameters of the 10M martensite in Ni–Mn-Ga alloys, which approach to the lattice parameter of the austenite phase as temperature increases, thus reducing the transformation strain. It is well known that Ni–Fe-Ga and Ni–Mn-Ga

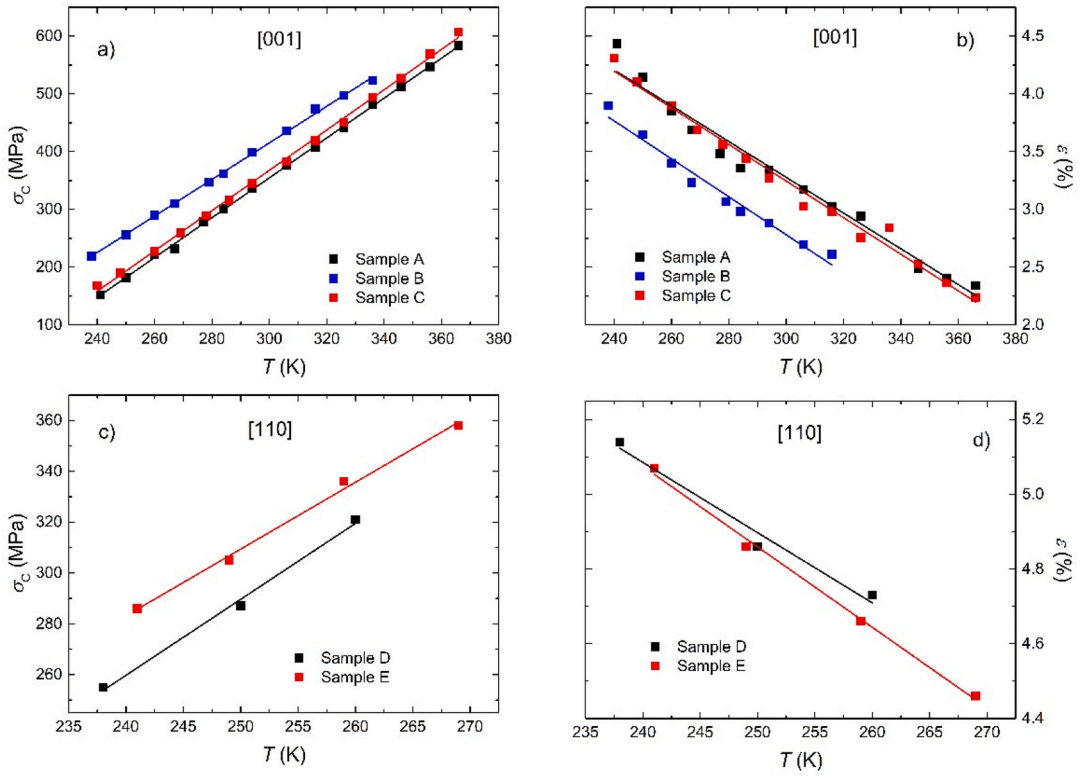

Fig. 5. Temperature dependence of the critical stress to start the transformation for samples tested in the (a) [001] and (c) [110] directions; and transformation strain for (b) [001] and (d) [110] directions, corresponding the forward martensitic transformation.

systems present many crystallographic analogies and equivalent martensitic phases, the 10M, 14M and 2M (also known as 5-layered, 7-layered and non-layered) being the most typical. Therefore, an evolution of the lattice parameters with temperature in the Ni–Fe-Ga Heusler alloys may be expected as well. Moreover, in both systems, the stress-induced martensite depends on the crystallographic orientation and the loading mode (tensile or compressive) and can be different from the thermal martensite [34,52]. The induced martensite phase can be inferred from the transformation strain, comparing with the theoretical strain $\varepsilon_{[hkl]}$ expected for each martensite. In a first approximation, the expected strains can be obtained from the Bain distortion between the austenite and martensite lattices. Using the lattice parameters of all phases in the crystallographic axes of the parent phase, the equations for the [001] and [110] orientations in compression are as follows:

$$\varepsilon_{[001]} = \frac{c_M - a_A}{a_A}$$

$$\varepsilon_{[110]} = \frac{\sqrt{b_M^2 + c_M^2} - \sqrt{2}\, a_A}{\sqrt{2}\, a_A}$$

where the subscripts A and M stand for austenite and martensite, respectively. The lattice parameters have been extracted from Ref. [20] (for the $Ni_{54}Fe_{19}Ga_{27}$ composition) and transformed into the unit cells corresponding to the crystallographic axes of austenite. Table 4 shows the transformed lattice parameters and the estimated theoretical strains for the 10M, 14M and 2M martensites. For the [001] orientation, the theoretical strains are very similar to those reported in Ref. [51], based on the energy minimization theory for the corresponding variant pair (CVP) strain + detwinning, which are also included in the table as reference. The transformation strain in the [001] direction is very similar for the three martensites, which makes difficult to discern which phase is induced by compression. This is not the case for the [110] orientation, with clear differences between the three martensites. Considering the experimental strain of 5.8% shown in Table 3, it becomes clear that the final martensite induced by compression along [110] is the 2M phase; though, as commented above, the irregular transformation paths suggest the existence of intermartensitic transformations, as reported in Refs. [51,52,54–56]. In order to shed some light on this point, the deformation between the first and second maxima in the loading curves has been measured for different temperatures in both samples, D and E. From this data a rough estimation of the deformation at M_s gives values of 2.6% and 2.8%, respectively, very close to the theoretical 2.9% of the 14M (see Table 4). This may support the formation of 14M martensite in the first stage followed by an intermartensitic transformation to 2M. As for the [001] orientation, the largest experimental strain achieved after extrapolation to the M_s temperature is 5.1% (Table 3), notably below the theoretical value expected for the three martensites (6.2–6.5%, Table 4). This result supports the possible formation of multivariant martensite due to the friction of the sample with the compression plates, reducing the experimental transformation strain and producing slight undulations of the stress-strain curve, as commented above.

Table 4
Lattice parameters of the austenite A and martensite (10M, 14M, 2M) phases extracted from Ref. [20] for $Ni_{54}Fe_{19}Ga_{27}$ and theoretical transformation strains, $\varepsilon_{[hkl]}$ calculated with Eq. 3 and 4 for both [001] and [110] directions.

	A ($L2_1$)	10M	14M	2M
a (nm)	0.576	0.602	0.613	0.654
b (nm)	0.576	0.592	0.580	0.539
c (nm)	0.576	0.538	0.538	0.539
$\varepsilon_{[110]}$ (%)		−1.8	−2.9	−6.4
$\varepsilon_{[001]}$ (%)		−6.5	−6.5	−6.4
$\varepsilon_{[001]}$ from Ref. [51] (%)		−6.38	−6.38	−6.25

3.3. Microstructural characterization after mechanical cycling

Samples A and C were used to investigate the microstructural changes after the mechanical cycles. Thin slices were cut from the central part of the compression samples and were prepared for TEM observation at room temperature under two-beam condition. According to the orientation of these samples, the thin foils are nearly parallel to the (001) plane (all indexes in this section correspond to the $L2_1$ unit cell). As typical in many SMA, the main effect of the mechanical cycling is the generation of dislocations. In the present alloy, a variety of distributions have been observed, which are compiled in Fig. 6. Some places contain only few individual dislocations with random location, as shown in Fig. 6(a), but it is quite often to find dislocation pile-ups forming thin bands, as illustrated in Fig. 6(b). In other areas, the density of dislocations is much higher and form complex arrays with erratic distribution (Fig. 6(c)) and even more dense accummulations in form of bands (Fig. 6(d)). The trace analysis of individual dislocations imaged in different zone axes allows to determine the crystallographic orientation of the dislocation line vector **u**. Most of the individual dislocations analyzed have **u** = <111> or **u** = <100>. To illustrate this result, the projections of these directions onto the image plane are indicated by black lines in all micrographs, whereas the zone axis and the **g** vector used for the two beam condition are marked in white color. Individual dislocations cross the thin foil from top to bottom. Then, the dislocations with **u** = [001] or [010] are nearly parallel to the thin foil and they project on the TEM image as long lines (see, for instance, the dislocations marked with A in Fig. 6(a) and (b)). In turn, dislocations with **u** = [001] are almost perpendicular to the foil and their projection is very short, as shown in Fig. 6(e).

The general criterion to determine the Burgers vector, **b**, is the extinction of contrast when the condition **g**·**b** = 0 is fulfilled [60]. However, for crystals with high elastic anisotropy, quantified by the constant $A = C_{44}/C'$, the invisibility criterion is not always satisfied and the Burgers vector has to be obtained by comparison with simulated images [61]. This method has been used in Cu-based SMA [62–65], with high values of the anisotropy constant (A = 12.8 for Cu-Zn-Al [62]). For ferromagnetic SMA, the elastic constants reported in Refs. [66,67] also give high anisotropy values of A = 6.6 and 9.2 for Ni–Fe-Ga and Ni–Mn-Ga, respectively. In the present study, full contrast extinction has only been observed for the long dislocations with **u** = [001] or [010]. To illustrate this result, Fig. 7 shows a series of micrographs of a group of dislocations in sample A taken under different **g** vectors. The long dislocation marked by A in Fig. 7(a), having **u** = [010], is well visible for all **g** vectors except for **g** = 040 (Fig. 7(c)), where the contrast disappears completey. The Burgers vector consistent with this extinction is **b** = ½[100], resulting in an edge dislocation. In turn, all other dislocations visible in Fig. 7 have **u** = <111> and do not show contrast extinction for any **g** vector. Fig. 8 shows another set of micrographs from an area of sample C, imaged under different **g** vectors. Individual dislocations with **u** = <111> or <100> can be distinguished, together with combined dislocations formed by several segments along <111> and <100>. Some of these combined dislocations are marked by A, B, C in Fig. 8(a). The long line marked by R, also visible in Fig. 8(b) and (c), does not correspond to a real crystal defect but to an artifact existing in the photographic plates (a careful inspection of these images shows that the line is located in different places of micrographs 8(a) to 8(c)).

Given the similar values of the elastic constants, we may consider that the simulated images for Cu–Zn–Al, shown in Refs. [62,63] are also valid for the present alloy. In fact, the dislocation contrast in Figs. 6–8 is very similar to the images reported in Refs. [62–65]. Like in Cu–Zn–Al, the comparison of experimental and simulated images confirms the Burgers vector **b** = ½<100> for the great majority of individual dislocations, for both line directions **u** = <111> and <100>.

In conclusion, the TEM study reveals that the dislocations generated by superelastic cycling in the $Ni_{51.5}Fe_{21.5}Ga_{27.0}$ alloy have Burgers vector of the type **b** = ½<100> and dislocation line directions **u** =

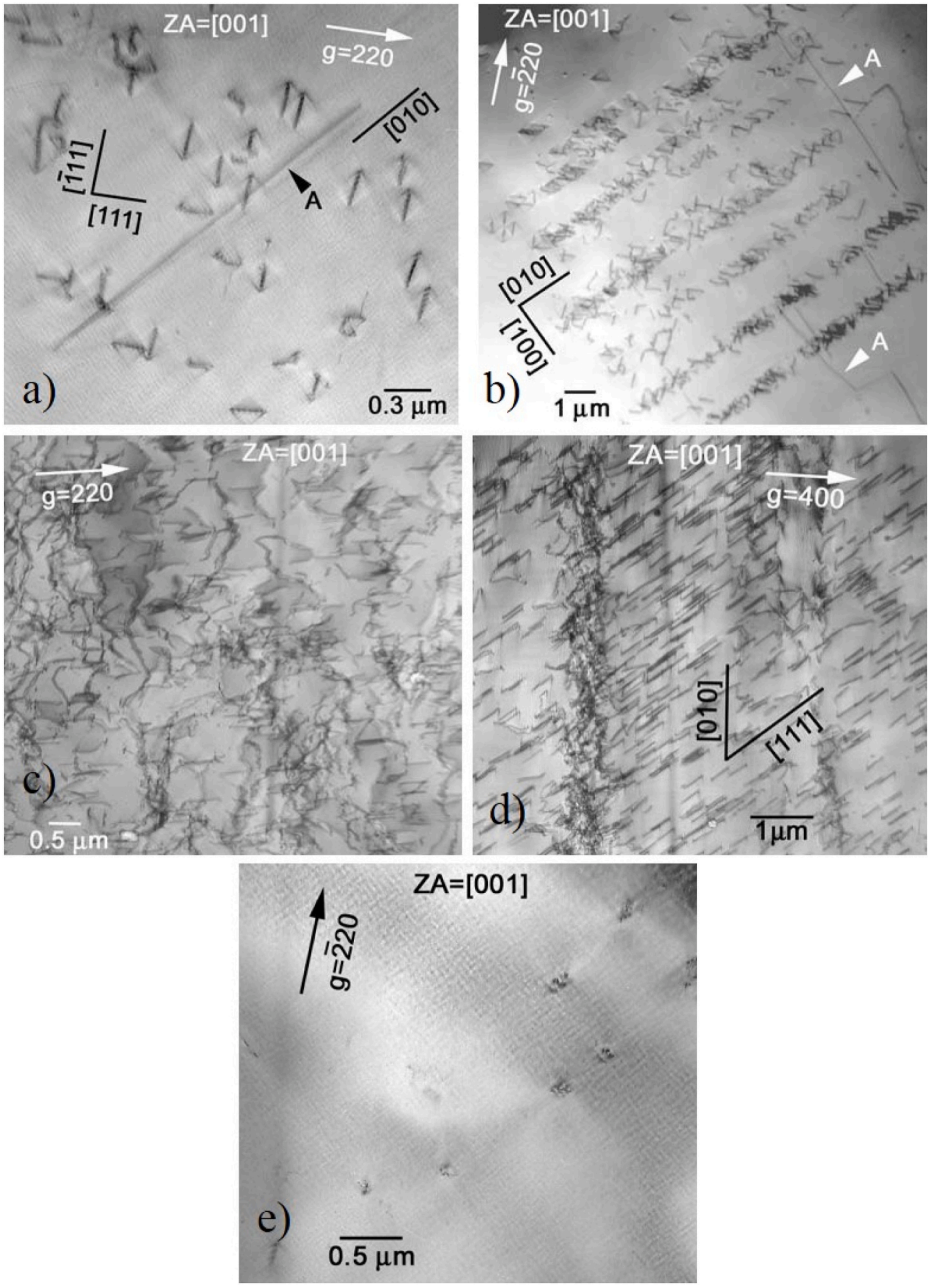

Fig. 6. Examples of different distributions of dislocations formed after mechanical cycling. (a) Individual dislocations with random locations (sample A). (b) Low magnification image with dislocation pile-ups forming parallel bands (sample A). (c) Area of sample C with a high densitiy of dislocations forming a complex array. (d) Distribution of dislocations in sample C forming a dense band in vertical direction. (e) Dislocations in sample A with direction **u** = [001], almost perpendicular to the thin foil.

<111> or <100>. These are the same crystallographic characteristics of the dislocations generated in Cu-based SMA by mechanical or thermal cycling [62–65]. As it is well known, the plastic deformation of bcc crystals occurs by slipping along the close packed direction <111> through dislocations with Burgers vector **b** = <111> as the main slip system. This was experimentally confirmed by Romero et al. [68] in Cu–Zn–Al SMAs with $L2_1$ austenite. The plasticity of martensite phase was also studied, and the dislocations observed had Burgers vectors corresponding to ½<100> in the $L2_1$ lattice, coincident with the dislocations formed by superelastic cyling. This result indicates that the later dislocations originate from plastic deformation of the martensite phase (see Refs. [69,70] and references therein). Unfortunately, no detailed studies of martensite plasticity have been done in Ni–Fe-Ga. However, the martensitic phases result from a distortion of the cubic $L2_1$ unit cell to an essentially tetragonal cell with $c/a<1$ for the 10M martensite, an orthorhombic cell for the 14M (disregarding the modulations with periodicities of 5 or 7 planes) or a tetragonal cell with $c/a>1$ for the 2M martensite [67]. In the three martensitic cells, one of the lattice parameters is shorter than in the parent phase. It is very likely that the plastic deformation of these martensites occurs by dislocations with **g** vectors along the shortest lattice parameter, which corresponds to the <100> direction of $L2_1$ austenite. Therefore, as this is the Burgers vector found in the present work and supported by the results on Cu–Zn–Al alloys mentioned above, it can be suggested that the dislocations formed by repetitive martensitic transformations are generated by plastic deformation of martensite. Due to the displacive nature of the martensitic transformation, the defects generated in martensite remain in austenite after the reverse transformation and are multiplicated by the repetitive mechanical cycling through the transformation. The superelastic cycles performed at low temperatures show complete recovery with no residual strain (Fig. 3), which indicates that only microplastic deformation of martensite occurs, probably as a result of the internal stresses generated by the intrinsic strain existing between both phases. Then, it can be assumed that the majority of the observed

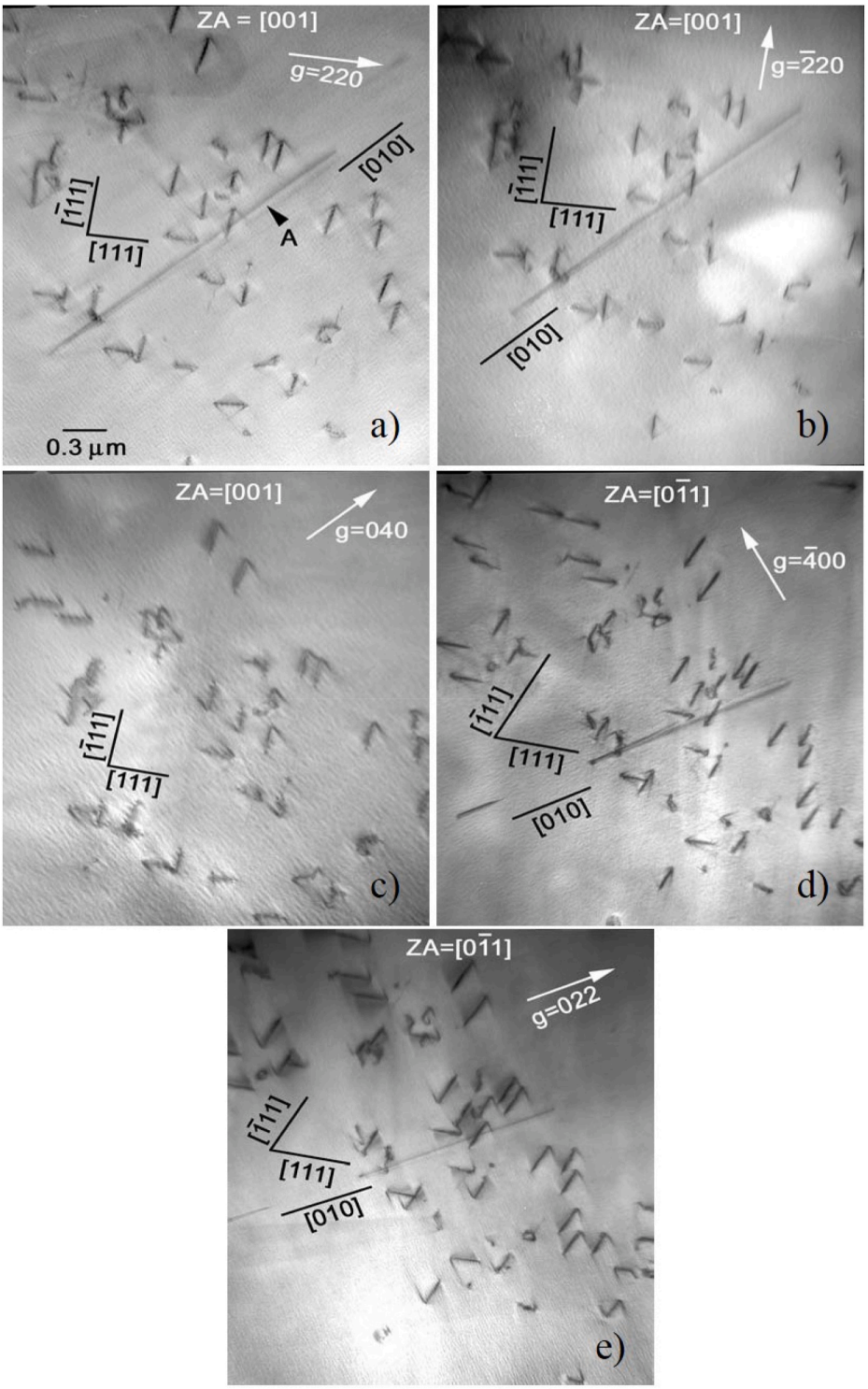

Fig. 7. Series of micrographs of the same area of sample A showing dislocations imaged under different **g** vectors.

dislocations are generated during the cycles performed at higher temperatures, for which the applied stress reaches higher levels and the material becomes softened by the effect of temperature. In this case, plastic deformation of martensite independent of the martensitic transformation strain could also occur and contribute to the residual strain observed in the $\sigma-\varepsilon$ curves at the highest test temperatures (Fig. 3).

3.4. Elastocaloric effect

The temperature change during loading and unloading in nearly adiabatic conditions has been measured in new samples C and E (with thermal treatment and orientation detailed in Table 1) at different temperatures to characterize the temperature and orientation dependences of elastocaloric properties. The measurements have been performed up to a high enough stress level for the transformation to be completed. The results obtained at 240 K are shown in Fig. 9(a). The

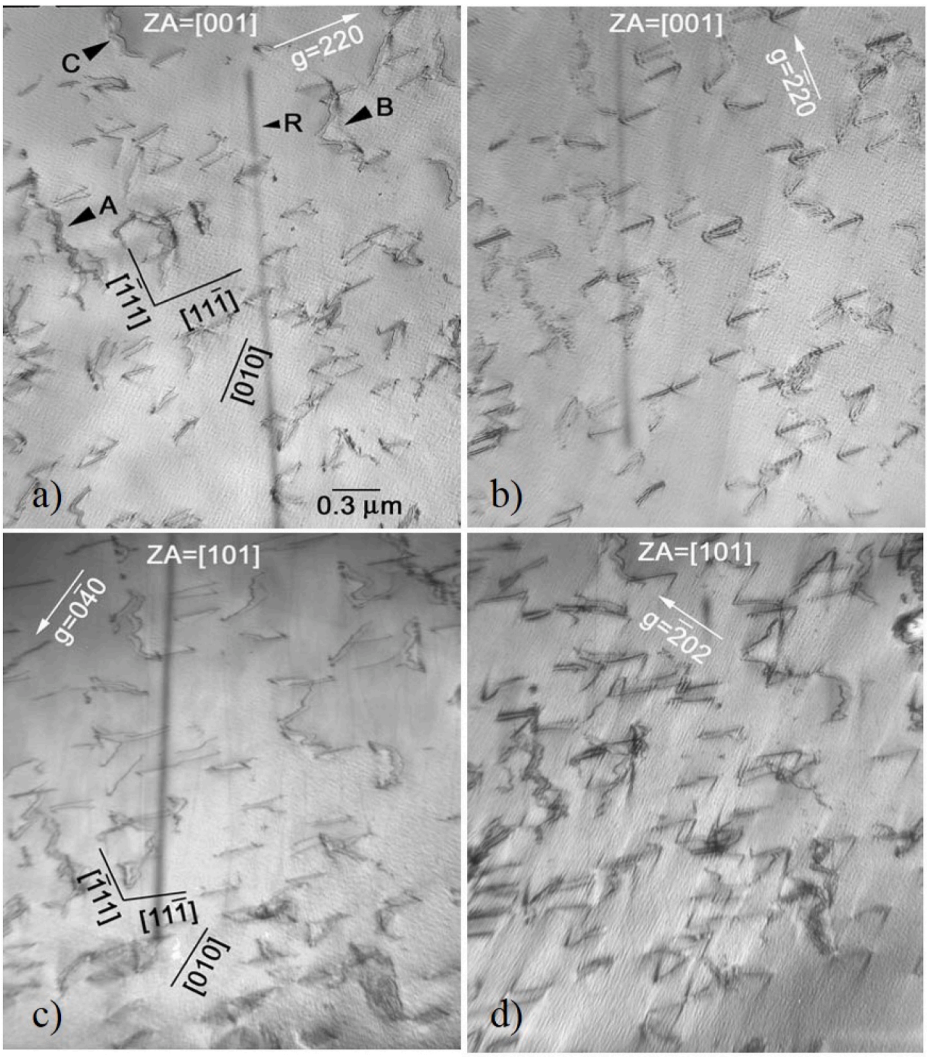

Fig. 8. Series of micrographs of the same area of sample C showing dislocations imaged under different **g** vectors.

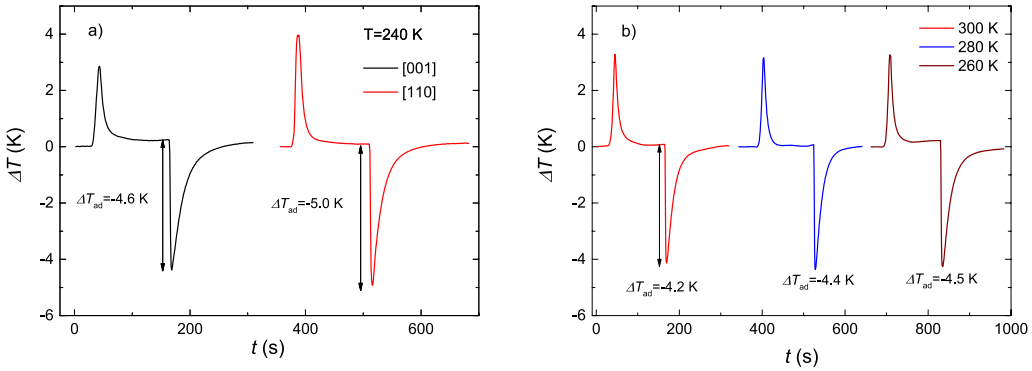

Fig. 9. Temperature change as function of time a) for samples C and E at $T = 240$ K, and b) for sample C at $T = 260$ K, 280 K and 300 K.

adiabatic cooling (ΔT_{ad}) measured during unloading at $\dot{\varepsilon} = 6{\cdot}10^{-2}\ s^{-1}$ is −5.0 K for [110] orientation and −4.6 K for [001], *i.e.* the effect is 0.4 K larger in the [110] orientation. This could be attributed to the notable differences in the transformation kinetics, as discussed in section 3.2, though it has to be noted that the transformation stress is larger in the [110] orientation with respect to the [001]. Fig. 9(b) shows the results obtained at 260 K, 280 K and 300 K only for the [001] sample. For the [110] orientation, the stress-induced transformation can not be reached due to previous fracture of the material. As shown in Fig. 9, the adiabatic cooling of [001] sample decreases by 0.4 K as the measurement temperature is increased from 240 K to 300 K. This reduction can be related to the decrease of transformation strain observed at increasing temperatures (Fig. 5(b)), together with the perfect linearity of the σ_c vs T dependence shown in Fig. 5(a). From the Clausius-Clapeyron equation, a reduction of ε must be compensated by a decrease of ΔS to keep a constant slope. This fact reduces the elastocaloric effect when the tests are

performed far from the M_s temperature. Pataky et al. [71] studied the elastocaloric properties of $Ni_{54}Fe_{19}Ga_{27}$ single crystal under compression along the [001] and [110] directions at room temperature. The obtained ΔT_{ad} values were 8.4 K and 7.6 K, respectively, *i.e.* the elastocaloric effect was larger for the [001] orientation, at difference with the present results. Similar values of adiabatic temperature change (7.5 K) were reported by Li et al. [46] in a [420]-oriented single crystal of the same composition. The $Ni_{54}Fe_{19}Ga_{27}$ composition has the transformation temperatures much closer to room temperature than the present alloy, which enhances the entropy change and adiabatic cooling obtained at room temperature. On its turn, Bruno et al. [51] investigated the elastocaloric effect from the entropy change calculated by integration of isothermal mechanical cycles and obtained similar ΔS values for [001] and [110] directions. All the results indicate that the main effect on the elastocaloric performance of Ni–Fe-Ga alloys is the distance from the M_s temperature of the alloy, whereas the crystallographic orientation has a minor influence.

4. Conclusions

The superelastic and elastocaloric effects of a $Ni_{51.5}Fe_{21.5}Ga_{27.0}$ single crystal in compression have been studied in this work, together with a detailed analysis of the dislocations formed after mechanical cycling. The main conclusions are as follows:

1. The $Ni_{51.5}Fe_{21.5}Ga_{27.0}$ single crystal presents a perfect superelasticity under compression along the [001] direction in a wide temperature window that extends up to ~ 160 K above the M_s temperature. Instead, for compression along [110], the superelastic window is much shorter due to the brittle fracture of the material.
2. The critical stress to start the transformation, σ_c, increases linearly with temperature for the whole superelastic window, whereas the experimental transformation strain decreases linearly with temperature. The origin of the latter effect is suggested to be related to the temperature dependence of the martensite lattice parameters. For both [001] and [110] orientations, the experimental slope of the σ_c vs. T line presents a good agreement with the Clausius-Clapeyron equation, using transformation strain values extrapolated to the M_s temperature and transformation entropy change values obtained from calorimetry data for the forward transition.
3. Heat treatments performed to retain high or low degrees of $L2_1$ atomic order, *i.e.* slow air cooling from 1070 K or water quenching from 970 K, respectively, produce the expected changes of the martensitic transformation temperatures according to Ref. [27]. High atomic order brings about a significant drop of transformation temperatures, whereas water quenching retain a low and inhomogeneous degree of order that widens the temperature range of transformation. Moreover, a previous solution heat treatment at 1420 K followed by water quench slightly enhances the order degree achieved after the subsequent thermal treatment due to the quenched-in vacancies. All effects of heat treatments observed in the thermal response of the material are translated to the mechanical stress-strain curves. The systematic shifts observed in the σ_c vs. T lines for different thermal treatments are in good correspondence with the changes of the martensitic transformation temperatures measured by DSC.
4. The Clausius-Clapeyron slope does not show significant variation with the degree of $L2_1$ atomic order of the parent phase, but a clear dependence on the orientation of the compression axis found. Values of 3.2–3.5 MPa K^{-1} for the [001] direction and 2.6–3.0 MPa K^{-1} for the [110] have been obtained in the $Ni_{51.5}Fe_{21.5}Ga_{27.0}$ single crystal.
5. The superelastic cycling generates dislocations in the material with irregular distribution and density within the sample volume. The dislocations have Burgers vector of the type $\mathbf{b}$ = ½<100> and dislocation line directions $\mathbf{u}$ = <111> (mixed dislocations) or <100> (edge dislocations). The Burgers vector obtained is incompatible with the plastic deformation of the $L2_1$ austenite and suggests that the dislocations are formed by plastic deformation of martensite. Once formed, the defects are inherited by the austenite phase due to the displacive character of the martensitic transformation.
6. The $Ni_{51.5}Fe_{21.5}Ga_{27.0}$ single crystal presents a significant elastocaloric effect related to the stress-induced transformation. The adiabatic cooling measured at 240 K during unloading at $\dot{\varepsilon} = 6{\cdot}10^{-2}$ s^{-1} is −5.0 K for [110] orientation and −4.6 K for [001]. At room temperature, the adiabatic cooling decreases to −4.2 K for [001] orientation, whereas the [110] sample suffers from brittle fracture before the stress-induced transformation. The decrease of the elastocaloric performance at increasing temperature is related to the decrease of the strain and entropy change of transformation. The cooling capacity of this alloy composition at room temperature is hindered by its low transformation temperatures. However, it can be a good option for applications at subambient temperatures.

Data availability

The data that support the findings of this study are available on request from the corresponding author.

CRediT authorship contribution statement

F. Masdeu: Conceptualization, Experimental work, Discussion of results. **J. Pons:** Conceptualization, TEM observations, Discussion of results, Writing – original draft, Funding acquisition. **J. Torrens-Serra:** Experimental Work, Discussion of results, Writing – original draft. **Y. Chumlyakov:** Production of single crystals, Conceptualization, Discussion of results. **E. Cesari:** Conceptualization, Discussion of results, Writing – review & editing, Funding acquisition.

Declaration of competing interest

The authors declare that they have no known competing financial interests or personal relationships that could have appeared to influence the work reported in this paper.

Ass. Prof. Torrens-Serra on behalf other authors.

Acknowlegdments

The work was supported by the Spanish “Ministerio de Ciencia, Innovación y Universidades - Agencia Estatal de Investigación (MCIU-AEI)” and “Fondo Europeo de Desarrollo Regional (FEDER), EU” under the project RTI 2018-094683-B-C51, and by the Ministry of Education and Science of the Russian Federation, Project N° 0721-2020-0022.

References

[1] H. Nagai, R. Oishi, Shape memory alloys as strain sensors in composites, Smart Mater. Struct. 15 (2006) 493–498, https://doi.org/10.1088/0964-1726/15/2/032.
[2] T. Waram, Actuator applications, in: V. Brailovski, S. Prokoshkin, P. Terriault, F. Trochu (Eds.), Shape Mem. Alloy. Fundam. Model. Appl., Université du Quebec, Quebec, 2003, pp. 731–754.
[3] M. Kohl, Y. Srinivasa Reddy, F. Khelfaoui, B. Krevet, A. Backen, S. Fähler, T. Eichhorn, G. Jakob, A. Mecklenburg, Recent progress in FSMA microactuator developments, Mater. Sci. Forum 635 (2009) 145–154. https://doi.org/10.4028/www.scientific.net/MSF.635.145.
[4] A. Cladera, B. Weber, C. Leinenbach, C. Czaderski, M. Shahverdi, M. Motavalli, Iron-based shape memory alloys for civil engineering structures: an overview, Construct. Build. Mater. 63 (2014) 281–293, https://doi.org/10.1016/j.conbuildmat.2014.04.032.
[5] P.K. Kumar, D.C. Lagoudas, SMAs as active materials — applications, in: D. C. Lagoudas (Ed.), Shape Mem. Alloy. Model. Eng. Appl., Springer US, Boston, MA, 2008, pp. 29–41, https://doi.org/10.1007/978-0-387-47685-8.
[6] J. Frenzel, G. Eggeler, E. Quandt, S. Seelecke, M. Kohl, High-performance elastocaloric materials for the engineering of bulk- and micro-cooling devices, MRS Bull. 43 (2018) 280–284, https://doi.org/10.1557/mrs.2018.67.

[7] L. Wei, X. Zhang, W. Gan, C. Ding, L. Geng, Hot extrusion approach to enhance the cyclic stability of elastocaloric effect in polycrystalline Ni-Mn-Ga alloys, Scripta Mater. 168 (2019) 28–32, https://doi.org/10.1016/j.scriptamat.2019.04.009.

[8] H. Sehitoglu, Y. Wu, E. Ertekin, Elastocaloric effects in the extreme, Scripta Mater. 148 (2018) 122–126, https://doi.org/10.1016/j.scriptamat.2017.05.017.

[9] A. Planes, L. Mañosa, M. Acet, Magnetocaloric effect and its relation to shape-memory properties in ferromagnetic Heusler alloys, J. Phys. Condens. Matter 21 (2009), 233201, https://doi.org/10.1088/0953-8984/21/23/233201.

[10] L. Mañosa, A. Planes, Materials with giant mechanocaloric effects: cooling by strength, Adv. Mater. 29 (2017), 1603607, https://doi.org/10.1002/adma.201603607.

[11] V.A. Chernenko, V.A. L'vov, E. Cesari, J.M. Barandiaran, Fundamentals of Magnetocaloric Effect in Magnetic Shape Memory Alloys, first ed., Elsevier B.V., 2019 https://doi.org/10.1016/bs.hmm.2019.03.001.

[12] K. Ullakko, J.K. Huang, C. Kantner, R.C. O'Handley, V.V. Kokorin, Large magnetic-field-induced strains in Ni_2MnGa single crystals, Appl. Phys. Lett. 69 (1996) 1966–1968, https://doi.org/10.1063/1.117637.

[13] A. Sozinov, N. Lanska, A. Soroka, W. Zou, 12% magnetic field-induced strain in Ni-Mn-Ga-based non-modulated martensite, Appl. Phys. Lett. 102 (2013), 021902, https://doi.org/10.1063/1.4775677.

[14] R. Kainuma, H. Nakano, K. Ishida, Martensitic transformations in NiMnAl β phase alloys, Metall. Mater. Trans. A Phys. Metall. Mater. Sci. 27 (1996) 4153–4162, https://doi.org/10.1007/BF02595663.

[15] M. Wuttig, J. Li, C. Craciunescu, A new ferromagnetic shape memory alloy system, Scripta Mater. 44 (2001) 2393–2397, https://doi.org/10.1016/S1359-6462(01)00939-3.

[16] K. Oikawa, L. Wulff, T. Iijima, F. Gejima, T. Ohmori, A. Fujita, K. Fukamichi, R. Kainuma, K. Ishida, Promising ferromagnetic Ni–Co–Al shape memory alloy system, Appl. Phys. Lett. 79 (2001) 3290–3292, https://doi.org/10.1063/1.1418259.

[17] K. Oikawa, T. Ota, T. Ohmori, Y. Tanaka, H. Morito, A. Fujita, R. Kainuma, K. Fukamichi, K. Ishida, Magnetic and martensitic phase transitions in ferromagnetic Ni–Ga–Fe shape memory alloys, Appl. Phys. Lett. 81 (2002) 5201–5203, https://doi.org/10.1063/1.1532105.

[18] J. Pons, E. Cesari, C. Seguí, F. Masdeu, R. Santamarta, Ferromagnetic shape memory alloys: alternatives to Ni-Mn-Ga, Mater. Sci. Eng. 481–482 (2008) 57–65, https://doi.org/10.1016/j.msea.2007.02.152.

[19] Z.H. Liu, G.H. Wu, Y. Liu, Stress-induced martensitic transformation of a $Ni_{54}Fe_{19}Ga_{27}$ single crystal in compression, Intermetallics 14 (2006) 1493–1500, https://doi.org/10.1016/j.intermet.2006.01.055.

[20] Y. Sutou, N. Kamiya, T. Omori, R. Kainuma, K. Ishida, K. Oikawa, Stress-strain characteristics in Ni–Ga–Fe ferromagnetic shape memory alloys, Appl. Phys. Lett. 84 (2004) 1275–1277, https://doi.org/10.1063/1.1642277.

[21] E.E. Timofeeva, E.Y. Panchenko, Y.I. Chumlyakov, H. Maier, Development of thermoelastic martensitic transformations in ferromagnetic [011]-oriented NiFeGa single crystals in compression, Russ. Phys. J. 54 (2012) 1427–1430, https://doi.org/10.1007/s11182-012-9766-9.

[22] R.F. Hamilton, C. Efstathiou, H. Sehitoglu, Y. Chumlyakov, Thermal and stress-induced martensitic transformations in NiFeGa single crystals under tension and compression, Scripta Mater. 54 (2006) 465–469, https://doi.org/10.1016/j.scriptamat.2005.10.003.

[23] R.F. Hamilton, H. Sehitoglu, C. Efstathiou, H.J. Maier, Inter-martensitic transitions in Ni-Fe-Ga single crystals, Acta Mater. 55 (2007) 4867–4876, https://doi.org/10.1016/j.actamat.2007.05.003.

[24] S. Belyaev, N. Resnina, V. Nikolaev, R. Timashov, A. Gazizullina, A. Sibirev, A. Averkin, V. Krymov, Shape memory effects in [001] $Ni_{55}Fe_{18}Ga_{27}$ single crystal, Smart Mater. Struct. 26 (2017), 095003, https://doi.org/10.1088/1361-665X/aa80c8.

[25] F. Masdeu, J. Pons, R. Santamarta, E. Cesari, J. Dutkiewicz, Effect of precipitates on the stress-strain behavior under compression in polycrystalline Ni-Fe-Ga alloys, Mater. Sci. Eng. 481–482 (2008) 101–104, https://doi.org/10.1016/j.msea.2006.10.213.

[26] F. Masdeu, J. Pons, C. Seguí, E. Cesari, J. Dutkiewicz, Some features of Ni-Fe-Ga shape memory alloys under compression, J. Magn. Magn Mater. 290–291 PA (2005) 816–819, https://doi.org/10.1016/j.jmmm.2004.11.371.

[27] R. Santamarta, E. Cesari, J. Font, J. Muntasell, J. Pons, J. Dutkiewicz, Effect of atomic order on the martensitic transformation of Ni–Fe–Ga alloys, Scripta Mater. 54 (2006) 1985–1989, https://doi.org/10.1016/j.scriptamat.2006.03.018.

[28] J. Font, J. Muntasell, R. Santamarta, J. Pons, E. Cesari, V. Recarte, J.I. Pérez-Landazábal, C. Gómez-Polo, J. Dutkiewicz, Thermal stability and ordering effects in Ni-Fe-Ga ferromagnetic shape memory alloys, Mater. Sci. Eng. 481–482 (2008) 262–265, https://doi.org/10.1016/j.msea.2007.01.183.

[29] R. Santamarta, J. Font, J. Muntasell, F. Masdeu, J. Pons, E. Cesari, J. Dutkiewicz, Effect of ageing on the martensitic transformation of Ni-Fe-Ga alloys, Scripta Mater. 54 (2006) 1105–1109, https://doi.org/10.1016/j.scriptamat.2005.11.062.

[30] H. Morito, A. Fujita, K. Fukamichi, R. Kainuma, K. Ishida, K. Oikawa, Magnetic-field-induced strain of Fe-Ni-Ga in single-variant state, Appl. Phys. Lett. 83 (2003) 4993–4995, https://doi.org/10.1063/1.1632039.

[31] H. Morito, K. Oikawa, A. Fujita, K. Fukamichi, R. Kainuma, K. Ishida, Enhancement of magnetic-field-induced strain in Ni–Fe–Ga–Co Heusler alloy, Scripta Mater. 53 (2005) 1237–1240, https://doi.org/10.1016/j.scriptamat.2005.08.009.

[32] H. Zheng, M. Xia, J. Liu, Y. Huang, J. Li, Martensitic transformation of $(Ni_{55.3}Fe_{17.6}Ga_{27.1})_{100-x}Co_x$ magnetic shape memory alloys, Acta Mater. 53 (2005) 5125–5129, https://doi.org/10.1016/j.actamat.2005.07.023.

[33] C. Efstathiou, H. Sehitoglu, P. Kurath, S. Foletti, P. Davoli, Fatigue response of NiFeGa single crystals, Scripta Mater. 57 (2007) 409–412, https://doi.org/10.1016/j.scriptamat.2007.04.049.

[34] Y. Chumlyakov, E. Panchenko, I. Kireeva, I. Karaman, H. Sehitoglu, H.J. Maier, A. Tverdokhlebova, A. Ovsyannikov, Orientation dependence and tension/compression asymmetry of shape memory effect and superelasticity in ferromagnetic $Co_{40}Ni_{33}Al_{27}$, $Co_{49}Ni_{21}Ga_{30}$ and $Ni_{54}Fe_{19}Ga_{27}$ single crystals, Mater. Sci. Eng. 481–482 (2008) 95–100, https://doi.org/10.1016/j.msea.2007.02.146.

[35] Y. Chumlyakov, I. Kireeva, E. Panchenko, I. Karaman, H.J. Maier, E. Timofeeva, Shape memory effect and high-temperature superelasticity in high-strength single crystals, J. Alloys Compd. 577 (2013) S393, https://doi.org/10.1016/j.jallcom.2012.02.003. –S398.

[36] Y.I. Chumlyakov, I.V. Kireeva, E.Y. Panchenko, V.A. Kirillov, E.E. Timofeeva, I. V. Kretinina, Y.N. Danil'son, I. Karaman, H. Maier, E. Cesari, Thermoelastic martensitic transformations in single crystals with disperse particles, Russ. Phys. J. 54 (2012) 937–950, https://doi.org/10.1007/s11182-011-9701-5.

[37] R.F. Hamilton, H. Sehitoglu, C. Efstathiou, H.J. Maier, Mechanical response of NiFeGa alloys containing second-phase particles, Scripta Mater. 57 (2007) 497–499, https://doi.org/10.1016/j.scriptamat.2007.05.024.

[38] C. Efstathiou, H. Sehitoglu, J. Carroll, J. Lambros, H.J. Maier, Full-field strain evolution during intermartensitic transformations in single-crystal NiFeGa, Acta Mater. 56 (2008) 3791–3799, https://doi.org/10.1016/j.actamat.2008.04.033.

[39] A. Kosogor, V.A. L'vov, V.A. Chernenko, E. Villa, J.M. Barandiaran, T. Fukuda, T. Terai, T. Kakeshita, Hysteretic and anhysteretic tensile stress–strain behavior of Ni–Fe(Co)–Ga single crystal: experiment and theory, Acta Mater. 66 (2014) 79–85, https://doi.org/10.1016/j.actamat.2013.11.064.

[40] V.A. Chernenko, V.A. L'vov, S. Kabra, I.R. Aseguinolaza, M. Kohl, H. Hosoda, J. M. Barandiaran, Large anhysteretic deformation of shape memory alloys at postcritical temperatures and stresses, Phys. Status Solidi 255 (2018), 1700273, https://doi.org/10.1002/pssb.201700273.

[41] E. Bonnot, R. Romero, L. Mañosa, E. Vives, A. Planes, Elastocaloric effect associated with the martensitic transition in shape-memory alloys, Phys. Rev. Lett. 100 (2008), 125901, https://doi.org/10.1103/PhysRevLett.100.125901.

[42] V. Recarte, J.I. Párez-Landazábal, C. Gómez-Polo, E. Cesari, J. Dutkiewicz, Magnetocaloric effect in Ni-Fe-Ga shape memory alloys, Appl. Phys. Lett. 88 (2006) 3–5, https://doi.org/10.1063/1.2189665.

[43] Y. Wu, E. Ertekin, H. Sehitoglu, Elastocaloric cooling capacity of shape memory alloys – role of deformation temperatures, mechanical cycling, stress hysteresis and inhomogeneity of transformation, Acta Mater. 135 (2017) 158–176, https://doi.org/10.1016/j.actamat.2017.06.012.

[44] M. Imran, X. Zhang, Ferromagnetic shape memory Ni-Fe-Ga alloy foams for elastocaloric cooling, J. Phys. D Appl. Phys. 53 (2020), 245503, https://doi.org/10.1088/1361-6463/ab7df1.

[45] M. Imran, X. Zhang, Elastocaloric effects in polycrystalline Ni-Fe-Ga foams with hierarchical pore architecture, Phys. Rev. Mater. 4 (2020), 065403, https://doi.org/10.1103/PhysRevMaterials.4.065403.

[46] Y. Li, D. Zhao, J. Liu, Giant and reversible room-temperature elastocaloric effect in a single-crystalline Ni-Fe-Ga magnetic shape memory alloy, Sci. Rep. 6 (2016) 1–11, https://doi.org/10.1038/srep25500.

[47] S. Belyaev, N. Resnina, V. Nikolaev, R. Timashov, A. Saveleva, A. Gazizullina, V. Krymov, A. Sibirev, Influence of detwinning on the shape memory effect in $Ni_{55}Fe_{18}Ga_{27}$ single crystals, J. Mater. Eng. Perform. 28 (2019) 4234–4240, https://doi.org/10.1007/s11665-019-04188-8.

[48] E.E. Timofeeva, E.Y. Panchenko, Y.I. Chumlyakov, A.I. Tagil'tsev, V.A. Kirillov, H. J. Maier, Special features of $L2_1$–L10 thermoelastic martensitic transformations in $Ni_{54}Fe_{19}Ga_{27}$ single crystals in tension, Russ. Phys. J. 61 (2018) 821–827, https://doi.org/10.1007/s11182-018-1465-8.

[49] N. Vetoshkina, E. Panchenko, E. Timofeeva, Y. Chumlyakov, N. Surikov, K. Osipovich, H. Maier, Effects of ageing on the cyclic stability of superelasticity in [001]-oriented $Ni_{49}Fe_{18}Ga_{27}Co_6$ single crystals in compression, in: Mater. Today Proc., 2017, pp. 4797–4801, https://doi.org/10.1016/j.matpr.2017.04.073.

[50] M. Imran, X. Zhang, M. Qian, L. Geng, Enhanced working stability of elastocaloric effects in polycrystalline Ni-Fe-Ga dual phase alloy, Intermetallics 136 (2021), 107255, https://doi.org/10.1016/j.intermet.2021.107255.

[51] N.M. Bruno, I. Karaman, Y.I. Chumlyakov, Orientation dependence of the elastocaloric effect in $Ni_{54}Fe_{19}Ga_{27}$ ferromagnetic shape memory alloy, Phys. Status Solidi Basic Res. 255 (2018) 1–11, https://doi.org/10.1002/pssb.201700437.

[52] E. Panchenko, Y. Chumlyakov, H.J. Maier, E. Timofeeva, I. Karaman, Tension/compression asymmetry of functional properties in [001]-oriented ferromagnetic NiFeGaCo single crystals, Intermetallics 18 (2010) 2458–2463, https://doi.org/10.1016/j.intermet.2010.09.009.

[53] N. Ozdemir, I. Karaman, N.A.A. Mara, Y.I.I. Chumlyakov, H.E.E. Karaca, Size effects in the superelastic response of $Ni_{54}Fe_{19}Ga_{27}$ shape memory alloy pillars with a two stage martensitic transformation, Acta Mater. 60 (2012) 5670–5685, https://doi.org/10.1016/j.actamat.2012.06.035.

[54] V. Nikolaev, G. Malygin, A. Averkin, S. Stepanov, G. Zograf, Anomalous stress-strain behaviour in $Ni_{49}Fe_{18}Ga_{27}Co_6$ crystals compressed along [110], Mater, Today Proc 4 (2017) 4807–4813, https://doi.org/10.1016/j.matpr.2017.04.075.

[55] V.I. Nikolaev, S.I. Stepanov, P.N. Yakushev, V.M. Krymov, S.B. Kustov, Burst-like shape recovery and caloric effects in Ni–Fe–Ga–Co single crystalline shape memory alloys, Intermetallics 119 (2020), 106709, https://doi.org/10.1016/j.intermet.2020.106709.

[56] D. Zhao, F. Xiao, Z. Nie, D. Cong, W. Sun, J. Liu, Burst-like superelasticity and elastocaloric effect in [011] oriented $Ni_{50}Fe_{19}Ga_{27}Co_4$ single crystals, Scripta Mater. 149 (2018) 6–10, https://doi.org/10.1016/j.scriptamat.2018.01.029.

[57] P. Wollants, J.R. Roos, L. Delaey, Thermally- and stress-induced thermoelastic martensitic transformations in the reference frame of equilibrium thermodynamics, Prog. Mater. Sci. 37 (1993) 227–288, https://doi.org/10.1016/0079-6425(93)90005-6.
[58] N. Glavatska, G. Mogylny, I. Glavatskiy, V. Gavriljuk, Temperature stability of martensite and magnetic field induced strain in Ni-Mn-Ga, Scripta Mater. 46 (2002) 605–610, https://doi.org/10.1016/S1359-6462(02)00019-2.
[59] I. Glavatskyy, N. Glavatska, I. Urubkov, J.U. Hoffman, F. Bourdarot, Crystal and magnetic structure temperature evolution in Ni-Mn-Ga magnetic shape memory martensite, Mater. Sci. Eng. 481–482 (2008) 298–301, https://doi.org/10.1016/j.msea.2007.02.139.
[60] P. Hirsch, A. Howie, R.B. Nicholson, D.W. Pashley, M.J. Whelan, Electron Microscopy of Thin Crystals, second ed., Robert Krieger Publishing Co, Florida (USA), 1977.
[61] A. Head, P. Humble, L. Clarebrough, A. Morton, C. Forwood, Computed Electron Micrographs and Defect Identification, North-Holland, Amsterdam, 1973.
[62] D.R. Jara, C. Esnouf, G. Guénin, A quantitative study of stable dislocations in the β1-phase of Cu-Zn-Al alloys, Phys. Status Solidi 87 (1985) 187–197, https://doi.org/10.1002/pssa.2210870119.
[63] M. Sade, A. Uribarri, F. Lovey, An electron-microscopy study of dislocation structures in fatigued Cu-Zn-Al shape-memory alloys, Philos. Mag. A. 55 (1987) 445–461, https://doi.org/10.1080/01418618708209908.
[64] J. Pons, F.C. Lovey, E. Cesari, Electron microscopy study of dislocations associated with thermal cycling in a Cu-Zn-Al shape memory alloy, Acta Metall. Mater. 38 (1990) 2733–2740, https://doi.org/10.1016/0956-7151(90)90287-Q.
[65] A. Ibarra, J. San Juan, E.H. Bocanegra, M.L. Nó, Evolution of microstructure and thermomechanical properties during superelastic compression cycling in Cu–Al–Ni single crystals, Acta Mater. 55 (2007) 4789–4798, https://doi.org/10.1016/J.ACTAMAT.2007.05.012.
[66] J.I. Pérez-Landazábal, V. Recarte, V. Sánchez-Alarcos, J.A. Rodríguez-Velamazán, M. Jiménez-Ruiz, P. Link, E. Cesari, Y.I. Chumlyakov, Lattice dynamics and external magnetic-field effects in Ni-Fe-Ga alloys, Phys. Rev. B Condens. Matter 80 (2009) 1–6, https://doi.org/10.1103/PhysRevB.80.144301.
[67] J. Pons, V.A.A. Chernenko, R. Santamarta, E. Cesari, Crystal structure of martensitic phases in Ni–Mn–Ga shape memory alloys, Acta Mater. 48 (2000) 3027–3038, https://doi.org/10.1016/S1359-6454(00)00130-0.
[68] R. Romero, F. Lovey, M. Ahlers, Plasticity in β phase Cu-Zn-Al alloys, Philos. Mag. A. 58 (1988) 881–903, https://doi.org/10.1080/01418618808214421.
[69] A. Cuniberti, R. Romero, M. Ahlers, The plastic deformation of long range ordered 18R martensitic single crystals of Cu-Zn-Al alloys, Scripta Metall. Mater. 26 (1992) 495–500, https://doi.org/10.1016/0956-716X(92)90636-S.
[70] C. Damiani, F.C. Lovey, M. Sade, Plastic deformation under compression of Cu–Zn–Al martensitic single crystals, Mater. Sci. Eng. 323 (2002) 436–444, https://doi.org/10.1016/S0921-5093(01)01380-6.
[71] G.J. Pataky, E. Ertekin, H. Sehitoglu, Elastocaloric cooling potential of NiTi, Ni_2FeGa, and CoNiAl, Acta Mater. 96 (2015) 420–427, https://doi.org/10.1016/j.actamat.2015.06.011.